AIAA JOURNAL
Vol. 42, No. 9, September 2004

Computation of Spinning Modal Radiation from an Unflanged Duct

X. Zhang,* X. X. Chen,† C. L. Morfey,‡ and P. A. Nelson§
University of Southampton, Southampton, England SO17 1BJ, United Kingdom

The radiation of high-order spinning modes from an unflanged duct with or without a mean flow is studied numerically. The application is to noise radiation from the intake duct of an aircraft engine. The numerical method is based on solutions of the linearized Euler equations (LEE) for propagation in the duct and near field and the acoustic analogy for far-field radiation. A formulation of the LEE is used for a single azimuthal mode, which offers an advantage in terms of computational efficiency: in the case of an axisymmetric mean flow-field, this model reduces computing costs connected with a three-dimensional model. In the solution process, acoustic waves are admitted from upstream into the propagation area surrounding the exit of an axisymmetric duct and the region immediately downstream. The wave admission is realized through an absorbing nonreflecting boundary treatment, which admits incoming waves and damps spurious waves generated by the numerical solutions. The wave propagation is calculated using a high-order compact scheme. Far-field directivity is estimated by solving the Ffowcs Williams–Hawkings equations. The far-field prediction is compared with analytic solutions, and good agreement is found.

I. Introduction

NOISE generation, propagation, and radiation from aircraft engines are governed by the Navier–Stokes equations. A full solution of the governing equations is not feasible at the moment. However, some aspects of the noise field can be studied separately. For example, sound propagation inside the inlet duct and radiation to the far field can be treated separately from the noise generation in the rotor/stator region, which requires solutions of the full nonlinear viscous equations. The former can be studied using equations linearized about a mean flowfield. This is a nontrivial problem, particularly in the high-frequency range, where typical length scales of the acoustic field are much less than the duct diameter.

Three main numerical methods have generally been used for the study of such problems: boundary-element (BE) schemes, finite element/infinite element (FE/IE) schemes, and computational-aeroacoustic (CAA) schemes based on the linearized Euler equations (LEE). The BE method[1] is restricted to acoustic disturbances in an irrotational mean flow. The FE/IE method solves the convected wave equations in the frequency domain.[2,3] It can be applied to acoustic disturbances propagating on an irrotational mean flow. Advantages are easy implementation of impedance boundary conditions and computational efficiency for two-dimensional and axisymmetric flows. CAA approaches,[4,5] based on either the full Euler equations or LEE, have advantages over the other two in that they admit entropic, vortical, and acoustic disturbances, and allow for arbitrary nonuniform mean flows. For the CAA methods, a finite computational domain is required, leading to the requirements of nonreflective acoustic boundary conditions and a radiation model, generally in the form of an integral representation.[6]

The present study is based on the CAA approach. CAA is concerned predominantly with obtaining time-accurate numerical solutions, through the use of long-time accurate time-integration strategies and high-order spatial discretization schemes. In pursuing this approach, we have in mind the problem of modal radiation from bypass and exhaust ducts of aircraft engines. In the near field in and around the duct exit, we model the noise propagation through LEE solutions. Under the assumption of axisymmetric mean flow, the disturbances can be represented by a series of Fourier components in the azimuthal direction. For a particular azimuthal mode, a system of two-dimensional equations can be used. Hence we are solving the so-called 2.5-dimensional form of the linearized Euler equations. For far-field radiation, we employ the Ffowcs Williams–Hawkings (FW-H) integral.[7,8] A canonical problem solved analytically by Homicz and Lordi[9] is used to validate the approach.

Presented as Paper 2002-2475 at the AIAA/CEAS 8th Aeroacoustics Conference, Breckenridge, CO, 17–19 June 2002; received 23 February 2003; revision received 3 March 2004; accepted for publication 19 March 2004.

*Professor of Aerodynamics, School of Engineering Sciences; xzhang@soton.ac.uk.
†Research Associate, Institute of Sound and Vibration Research.
‡Emeritus Professor, Institute of Sound and Vibration Research.
§Professor of Acoustics, Institute of Sound and Vibration Research.

II. Governing Equations

Assuming small perturbations about a steady mean flow, acoustic wave propagation can be described by the linearized Euler equations in a cylindrical coordinate system, which take the form

$$\frac{\partial \rho'}{\partial t} + \nabla \cdot (\rho' \boldsymbol{V}_0 + \rho_0 \boldsymbol{V}') = 0 \tag{1}$$

$$\frac{\partial u'}{\partial t} + \boldsymbol{V}_0 \cdot \nabla u' + \boldsymbol{V}' \cdot \nabla u_0 + \frac{\partial p'}{\rho_0 \partial x} = 0 \tag{2}$$

$$\frac{\partial v'}{\partial t} + \boldsymbol{V}_0 \cdot \nabla v' + \boldsymbol{V}' \cdot \nabla v_0 + \frac{\partial p'}{\rho_0 \partial y} = 0 \tag{3}$$

$$\frac{\partial w'}{\partial t} + \boldsymbol{V}_0 \cdot \nabla w' + \boldsymbol{V}' \cdot \nabla w_0 + \frac{\partial p'}{\rho_0 y \partial \theta} = 0 \tag{4}$$

$$\frac{\partial p'}{\partial t} + \boldsymbol{V}_0 \cdot \nabla p' + \boldsymbol{V}' \cdot \nabla p_0 + \gamma (p_0 \nabla \cdot \boldsymbol{V}' + p' \nabla \cdot \boldsymbol{V}_0) = 0 \tag{5}$$

Here $(\rho', \boldsymbol{V}', p')$ are density, velocity, and pressure perturbations; $(\rho_0, \boldsymbol{V}_0, p_0)$ are mean flow properties; u is the axial velocity; v the radial velocity; w the azimuthal velocity; x and y are axial and radial coordinates; and θ is the azimuthal angle. The fluid is modeled as a perfect gas, and all variables are nondimensionalised using a reference length L^*, a reference sound speed a^*, and a reference density ρ^*. For the numerical examples presented next, these have been taken as 1 m, 340 m/s, and 1.225 kg/m^3.

Solutions of the preceding equations require three-dimensional codes and are expensive. If we were to assume that the acoustic disturbances are restricted to multiples of the blade passing frequency and propagate on an axisymmetric mean flowfield without swirl, it

would be possible to write the disturbances in terms of a Fourier series, for example, for the axial velocity disturbance u' at a single frequency

$$u' = \sum_m u'_m(x, y)e^{i(kt - m\theta)} \tag{6}$$

It is now possible to express the overall disturbances in terms of the sum of individual components. Each individual component (mode) can be described by a set of two-dimensional equations. Generally the equations are solved in complex form. However, if we utilize Eq. (6), then it is possible to arrive at a new set of equations in which i does not appear:

$$\frac{\partial \rho'}{\partial t} + u_0\frac{\partial \rho'}{\partial x} + \rho_0\left(\frac{\partial u'}{\partial x} + \frac{\partial v'}{\partial y} - \frac{m}{ky}w'_t + \frac{v'}{y}\right) = 0 \tag{7}$$

$$\frac{\partial u'}{\partial t} + u_0\frac{\partial u'}{\partial x} + \frac{\partial p'}{\rho_0 \partial x} = 0 \tag{8}$$

$$\frac{\partial v'}{\partial t} + u_0\frac{\partial v'}{\partial x} + \frac{\partial p'}{\rho_0 \partial y} = 0 \tag{9}$$

$$\frac{\partial w'_t}{\partial t} + u_0\frac{\partial w'_t}{\partial x} + \frac{mk}{\rho_0 y}p' = 0 \tag{10}$$

Equation (4) has been recast in terms of $w'_t(= \partial w/\partial t)$. Solutions of the new 2.5-dimensional equations require only two extra arrays for $w'^{(i)}_t$ and $w'^{(i+1)}_t$, where i stands for time step. The boundary treatment for w'_t is the same as that for w'. Therefore Eq. (10) does not change the form of Eq. (4). The code implementation is easy. The w' velocity is recovered after each time step.

An integral solution of the FW-H equation is implemented numerically to allow the near and far-field noise levels to be determined efficiently.[10] The particular integral solution implemented is known as formulation 1A following Farassat and Succi.[7] Earlier studies showed that the placement of the FW-H integration surface has only a small effect on the far-field directivity.[8,11]

III. Radiation of High-Order Spinning Modes

We use as a test case the modal radiation (with and without uniform mean flow) from an unflanged duct, described by Homicz and Lordi[9] (Fig. 1). In Fig. 1, M_∞ is defined as the scaled mean flow velocity. The far-field sound level and directivity from the analytical solution and near-field sound levels from FE schemes can be used for validation purposes. Earlier work[11] has concentrated on nonspinning (axisymmetric) modal radiation in order to test the numerical method. Good agreement between numerical and analytical solutions has been found.

We look at a single (m, n) mode, where azimuthal mode number is denoted by m, propagating and radiating from a semi-infinite unflanged duct with thin rigid walls. The index n denotes the radial mode order, with the lowest order mode labeled $n = 1$. The incident wave is defined as follows:

$$p' = \mathrm{Re}\{aJ_m(k_r y)\exp[\mathrm{i}(kt - k_a x - m\theta)]\}$$

$$u' = \frac{k_a}{k - k_a M_\infty}p'$$

$$v' = \mathrm{Re}\left\{\frac{a}{k - k_a M_\infty}\frac{\mathrm{d}J_m(k_r y)}{\mathrm{d}y}\exp[\mathrm{i}(kt - k_a x - m\theta + \pi/2)]\right\}$$

$$w'_t = \mathrm{Re}\left\{-\frac{mkaJ_m(k_r y)}{y(k - k_a M_\infty)}\exp[\mathrm{i}(kt - k_a x - m\theta + \pi/2)]\right\}$$

where the dimensionless modal amplitude a is fixed at 10^{-4} to ensure small relative changes in density (as required for LEE). The radial wave number k_r is determined by turning points of the Bessel function, and the axial wave number k_a and cuton ratio ξ are calculated from

$$k_a = (k/\beta^2)\left(-M_\infty \pm \sqrt{1 - \xi^{-2}}\right), \qquad \xi = k/k_r\beta$$

where $\beta = \sqrt{1 - M_\infty^2}$.

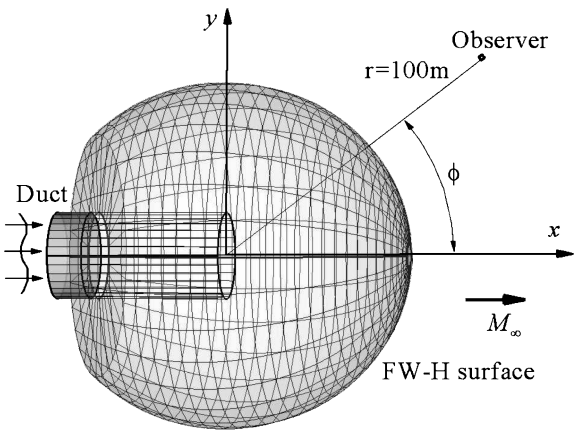

Fig. 1 Schematic of duct test case setup.

IV. Numerical Methods

The LEE solver uses a sixth-order compact scheme[12] for spatial derivatives and a fourth-order 4/6 stage explicit Runge–Kutta scheme[13] for time integration. A 10th-order filter is also applied at each stage of the Runge–Kutta scheme.[14] A slip-wall boundary condition is applied to the duct wall, and buffer zones are placed around the boundary of the physical computational domain to provide nonreflecting boundary conditions. Inside the duct, a buffer zone (with a width of at least one wavelength λ_a) is used to absorb the spurious waves as well as to act as an admission region, where the incident wave is used as reference. Elsewhere in the surrounding buffer zones, the waves are damped to zero at the buffer zone outer boundary. Only two-dimensional problems are considered here. However the application to three-dimensional problems is straightforward. The basic methodology has been validated against a range of test cases, including a Gaussian acoustic pulse diffracted by a two-dimensional cylinder.[12] The two-dimensional method developed for single spinning-mode propagation has also been validated against a simple duct case.

In presenting the results, unless otherwise stated, nondimensional values will be used. The diameter of the duct is taken as two units. The length of the duct is fixed at 1.5. The origin of the coordinate system is placed at the center of the duct exit. The axial extent of a typical computation domain ranges from -1.5 to 3 and the radial extent from 0 to 3. A three-dimensional FW-H surface is constructed to evaluate the far-field noise level. Comparison with Homicz and Lordi[9] is made at a diameter of 100 m from the duct axis. The solutions cover an arc of 120 deg consisting of 100 points.

V. Results and Discussion

A. Modal Propagation in Duct

To test the resolution requirement, the propagation of a single mode inside a circular duct with hard-wall boundary condition is tested. The duct has a radius of 1, and the computation covers an axial distance of 2.5. Two cases are selected: 1) $m = 13$, $k = 23$, $\xi = 1.54$ and 2) $m = 30$, $k = 40$, $\xi = 1.23$.

Both stretched and unstretched grids are used in the computation. We have explored the possibilities of improving the resolution near the duct wall and at the exit. The grid is stretched in the radial direction to improve the points per wavelength near the wall. The stretching is based on the following function:

$$y_j = y_1 + (y_{my} - y_1)\left[1 - \alpha + \frac{2\alpha}{1 + (\alpha + 1)^\eta/(\alpha - 1)^\eta}\right] \tag{11}$$

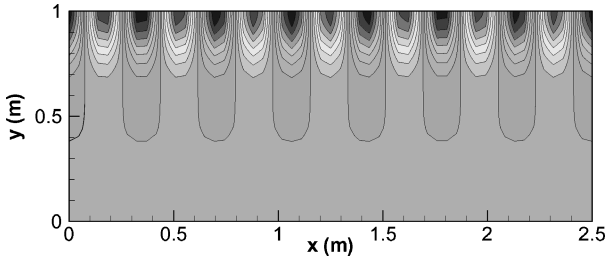

Fig. 2 Wave propagation pattern: $m = 13$, $n = 1$, $k = 23$, $\xi = 1.54$, and $M_\infty = 0$.

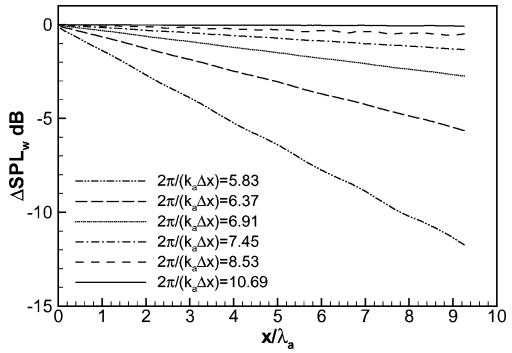

a) Sound pressure level on the duct wall: $m = 30$, $n = 1$, $k = 40$, $\xi = 1.23$

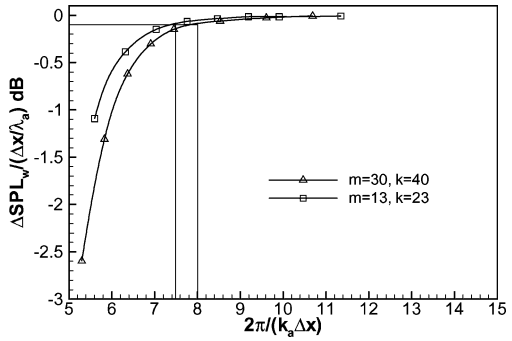

b) Sound pressure level decay per wavelength

Fig. 3 Axial resolution requirement for duct modal propagation: $2\pi/(k_r\Delta y) = 15.2$.

where $\alpha > 1$ is the compression ratio and $\eta = (m_y - j)/m_y$. In the duct computation and radiation computation, the cell size in the buffer zone region is kept constant.

Figure 2 gives an example of wave propagation patterns (pressure) inside the duct. The axial resolution is kept at $2\pi/(k_a\Delta x) = 10.8$, and the radial resolution is kept at $2\pi/(k_r\Delta y) = 15.7$. The grid is stretched in the radial direction with $\alpha = 1.05$. Visual inspection suggests that this specification is more than adequate. A quantitative description of the resolution requirement is given in Fig. 3a, where the pressure decay on the wall is plotted over an axial distance of about nine wavelengths (λ_a). In obtaining the results in Fig. 3, the cell distribution in the radial direction is fixed at an average $2\pi/(k_r\Delta y) = 15.2$ with a compression ratio of 1.05. It can be seen that with lower $2\pi/(k_a\Delta x)$ a larger decay is experienced along the axial direction. The solution improves as $2\pi/(k_a\Delta x)$ is increased.

Defining a criterion for resolution is an arbitrary process. If we specify a requirement of sound pressure level (SPL) decay per wavelength, $|\mathrm{d}(\mathrm{SPL}_w\ \mathrm{dB})/\mathrm{d}(x/\lambda_a)| < 0.1$ dB, an axial resolution of between 7 and 8 appears to be adequate (Fig. 3b).

To test the grid resolution requirement in the radial direction, we have used an axial resolution of $2\pi/(k_a\Delta x) = 10.7$ and changed the cell distribution in the radial direction. A compression ratio of 1.05 is used in this series of tests. Results are presented in Fig. 4a. Again an average resolution requirement of $2\pi/(k_r\Delta y) = 7 - 8$ seems adequate for $|\mathrm{d}(\mathrm{SPL}_w\ \mathrm{dB})/\mathrm{d}(x/\lambda_a)| < 0.1$ dB. The number used in Fig. 4a, though, is the averaged value. If a uniform grid were employed, then this criterion would not be met. In fact if we were to use an unstretched grid and keep the resolution at $2\pi/(k_r\Delta y) = 10.8$, we would have decay ratio of $|\mathrm{d}(\mathrm{SPL}_w\ \mathrm{dB})/\mathrm{d}(x/\lambda_a) = -0.56$ dB. To meet the decay criterion, a minimum resolution near the wall must be satisfied. Figure 4b suggests that a minimum value of $2\pi/(k_r\Delta y) = 30$ is required near the wall.

Table 1 Test cases

Frequency	$m = 13$, $M_\infty = 0$			$m = 13$, $M_\infty = -0.5$			$m = 30$, $M_\infty = 0$		
k	15	23	30	15	23	30	33	40	50
ξ	1.01	1.54	2.10	1.16	1.78	2.32	1.01	1.23	1.54
f, Hz	812	1245	1623	812	1245	1623	1786	2165	2706

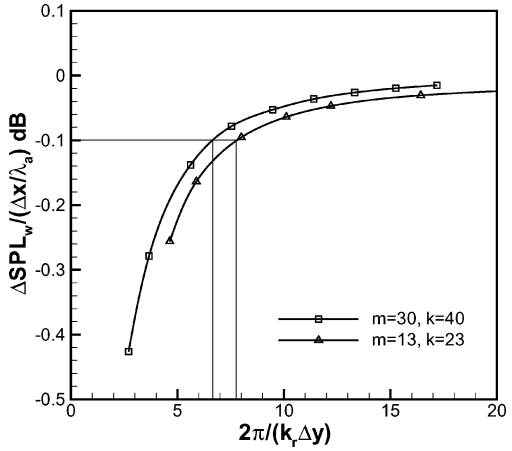

a) Sound pressure level decay per wavelength on the duct wall: $2\pi/(k_a\Delta x) = 10.7$

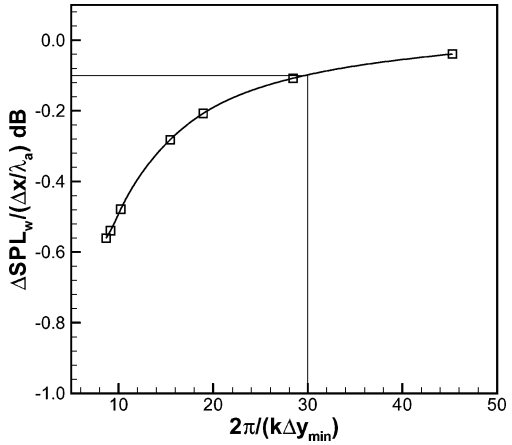

b) Resolution requirement near the wall: $2\pi/(k_a\Delta x) = 10.7$, $2\pi/(k_r\Delta y) = 10.8$

Fig. 4 Radial resolution requirement for duct modal propagation.

B. Radiation from a Semi-Infinite Duct

For the radiation tests, we have selected two high-order spinning-mode radiation cases. Detailed conditions are listed in Table 1. In addition to the cases listed, we have also studied $m = 30$, $M_\infty = -0.5$ cases, and $m = 13$ at $M_\infty = 0.1$, 0.2, 0.25, and 0.3. As the $m = 30$ results are similar to the $m = 13$ ones, we will not include them in the paper. These cases are studied to consider the effect of changing m and Mach number.

We have used weakly stretched grids in this study. For all of the cases, the compression ratio of the grid is 1.25. Care was taken to meet the minimum grid resolution near the wall and elsewhere in the computation domain. Unless otherwise stated, a minimum resolution of $2\pi/(k_r\Delta y_{\min}) = 2\pi/(k_a\Delta x_{\min}) = 30$ is used near the wall, and $2\pi/(k_r\Delta y) = 2\pi/(k_a\Delta x) > 10$ elsewhere.

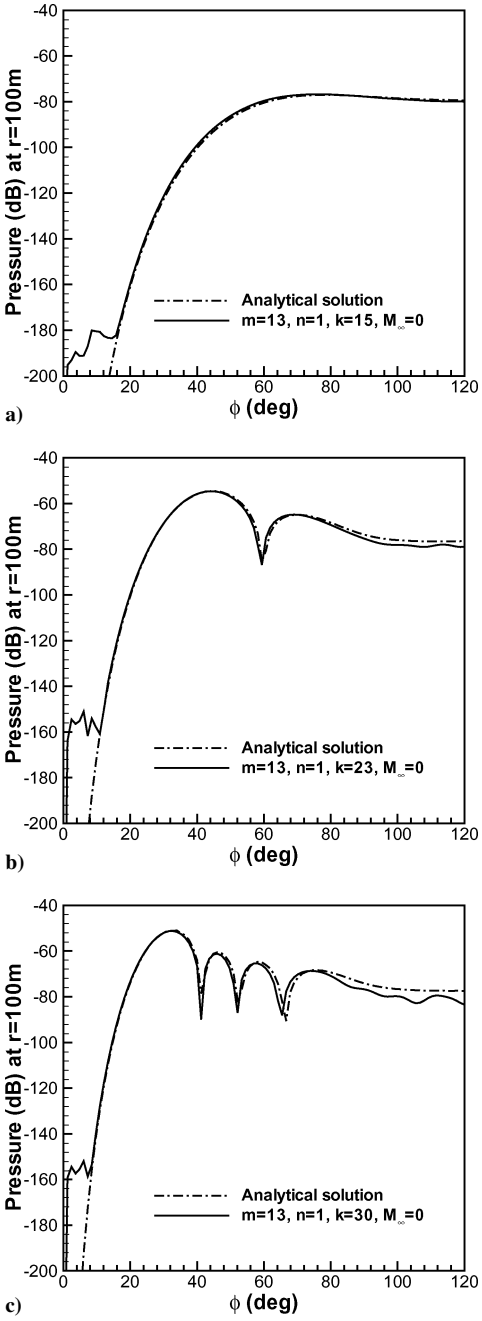

Fig. 5 Far-field directivity for the $m = 13$ modal radiation at a) $k = 15$, $\xi = 1.01$; b) $k = 23$, $\xi = 1.54$; and c) $k = 30$, $\xi = 2.01$: $M_\infty = 0$.

The appropriate measure for judging the quality of the computation is the far-field directivity pattern. In Fig. 5 the predicted far-field pressures are compared with the analytical solutions.[9] It appears that both the peak level and peak angle are predicted well by the current method. At $k = 15$, the mode in the duct is near cutoff. Hence we only observe weak radiation. Nevertheless, the radiation pattern is predicted well. The predicted peak pressure is within 0.28 dB of the analytical solution.[9] The peak angle is predicted to within 2.4 deg. At low angles to the duct axis ($0 < \phi < 16$ deg), the numerical prediction fails to follow the decaying envelope. This particular feature is limited by the numerical accuracy of the CAA scheme (see later). However, the prediction does cover a dynamic range of approximately 100 dB. The overall accuracy suffers slightly as the observation angle approaches 120 deg, the discrepancy in pressure level being at most 0.5 dB.

At $k = 23$, the cutoff ratio is 1.54. Two radiation peaks now appear at $\phi = 44.85$ and 70.30 deg, separated by a shadow interference dip angle at 59.39 deg. The predicted peak angles are at 43.64 and 69.09 deg, well within the error introduced by the discrete observation positions. The first peak in the pressure level is −54.64 dB, at 0.23 dB below the analytical prediction. The second peak is at −64.84, which is only 0.09 dB above the analytical prediction. Towards the larger observation angle, the discrepancy in the pressure level again increases slightly, being at 2.3 dB below the analytical solution at $\phi = 120$ deg. This feature is the same as the $k = 15$ case. Again the dynamic range of the prediction is about 100 dB. At the high cutoff ratio of 2.01 ($k = 30$), the quality of the prediction remains the same.

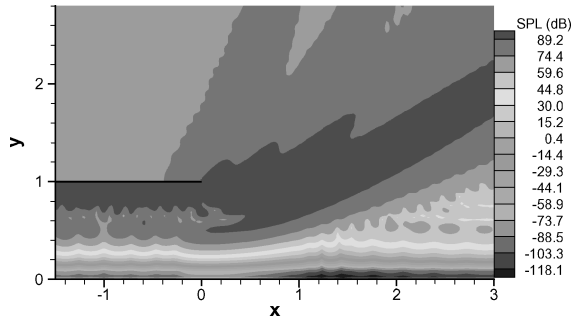

Fig. 6 Sound pressure level for the $m = 13$, $n = 1$ modal radiation: $k = 30$, $\xi = 2.01$, and $M_\infty = 0$.

Another indicator of prediction quality is provided by contours of the near-field sound pressure level. An example is given in Fig. 6, calculated over one period of wave propagation. Several interesting features are highlighted by the SPL contours. These show upstream-propagating waves initiated at the edge of the duct, which are obvious at $k = 23$ (not shown) and 30. At the lower frequency of $k = 15$ (not shown), this feature is not so strong. The boundary condition employed for this study (i.e., the wave admission region inside the duct) has effectively absorbed the upstream traveling waves.

The basic radiation patterns are illustrated by the high-SPL lobes emanating from the edge of the duct. Inside the duct as well as near the duct exit, the SPL contours are reasonably smooth. However, as the waves propagate farther away from the duct, regular standing wave patterns begin to appear. These wave patterns should be considered separately from those inside the duct, which are produced by reflections from the edge of the duct. They could be caused by the spurious wave reflection from the computation boundaries, as one might suspect. In tests conducted with various placements and treatment of the buffer zone, absorbing boundary conditions reduced the adverse effect of these waves on the far-field directivity prediction but did not completely eliminate the standing waves. These standing waves are of lower level. Their appearance could also be attributed to the dispersion characteristics of the sixth-order compact scheme.[15] They do contribute to the "leakage" at the low observation angle and nonphysical "wiggles" at high observation angles in the far-field directivity prediction.

The high-order spinning mode radiation at $m = 30$ presents a much more stringent test than the $m = 13$ case. For this modal radiation problem, we again select three cutoff ratios at 1.01, 1.23, and 1.54. An example of the far-field directivity predictions is given in Fig. 7. Results are rather similar to those achieved for the $m = 13$, $M_\infty = 0$ case. For this mode, the highest radiation peaks are at 77.58 deg for $k = 33$, 58.18 deg for $k = 40$ and 43.64 deg for $k = 50$. The predicted values are 76.37, 58.18, and 42.42 deg, respectively. To the left of the main radiation peak, the pressure level drops off quickly as the observation angle becomes smaller. Below the 100-dB dynamic range of the prediction, the pressure level again is not predicted. Generally, the directivity pattern around the main peak radiation is predicted well, which includes both the level and the angle. The shadow interference dip angles are also well predicted. Discrepancies are within the positional error introduced by the discrete far-field monitoring stations, of which 100 points are employed to over an 120-deg arc. A feature of the prediction, though, is the slight deterioration towards the high observation angle range. This will be discussed further later. The standing wave patterns in the

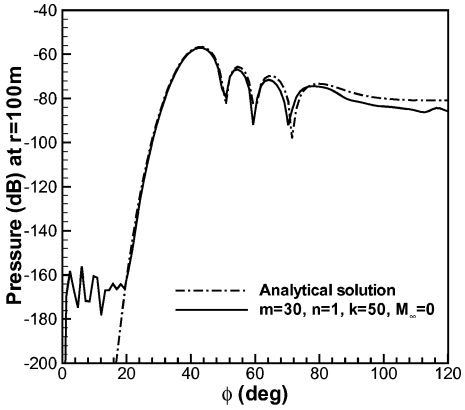

Fig. 7 Far-field directivity for the $m = 30$, $n = 1$ modal radiation at $k = 50$, $\xi = 1.54$: $M_\infty = 0$.

SPL contours have a small influence on the overall quality of the prediction.

Introducing a uniform flow will not alter the radial wave number k_r but will increase the axial wave number k_a, thereby placing much tougher requirement on grid resolution. For the $m = 13$ modal radiation, introducing a $M_\infty = -0.5$ uniform flow will increase the axial wave number from 1.5 to 20.1 at $k = 15$, 17.5 to 40.7 at $k = 23$ and 26 to 56.1 at $k = 30$. As the wavelength reduces, the size of the grid cell must be reduced as well to achieve the same level of $2\pi/(k_a \Delta x)$ requirement. Results of the prediction are given in Figs. 8 and 9 in terms of directivity and SPL. In terms of quality of the prediction, the same type of conclusions can be drawn as for the $M_\infty = 0$ cases. Both the major radiation peaks and the main interference dip angles are predicted well. The prediction deteriorates slightly toward the high observation angles. This is particularly true for the $m = 30$ case. The dynamic range of the prediction remains at 100 dB. For a nearly cuton mode ($k = 13$), the shape and the level of the main radiation peak are changed. For the well cuton modes at ($k = 23$ and 30), the effect of a higher oncoming Mach number is seen to introduce additional radiation peaks at higher observation angles, as shown by the pressure waves in Fig. 9. The level of the main radiation peak remains nearly the same. This feature is well predicted by the current method.

C. Discussion

A common feature of the far-field directivity prediction is the slight deterioration in the pressure level at higher observation angles. This deterioration is only relative to the main radiation peak prediction, which is always good. The radiation at the higher angles is inevitably linked to scattering from the edge of the duct. Hence in addressing the quality of the prediction, we need to look at two issues: the treatment of the duct exit and the grid resolution near the exit. To help clarify the problem, we conduct three exercises: one with different duct-edge geometry and another with different grid resolution near the duct edge and placement of the integral surface.

For the duct-edge geometry study, the modal radiation test case is that of $m = 13$, $k = 23$, and $M_\infty = 0$. Two types of duct edge are used: a rectangular edge of finite thickness and a chamfered wedge. Results in terms of the far-field directivity are given in Fig. 10. Compared with the datum case of zero wall thickness, the 15-deg wedge does not introduce any significant changes in the radiation pattern (Fig. 10a). Changes in the angle of the wedge do not alter the main radiation peak and the interference dip angle. The leakage in the low observation angle as discussed earlier is not affected (not shown). At high observation angle, there is a perceptible change in the far-field directivity with a small bump appearing at around 105 deg. The rectangular exit has a bigger effect on the second radiation peak. Increasing the thickness of the wall from 4 to 8% of the duct diameter shifts the predicted pressure level up by 1.5 dB. The angle, though, remains the same. Again, the main influence is in the high observation angle range rather than the low observation angle range (not shown).

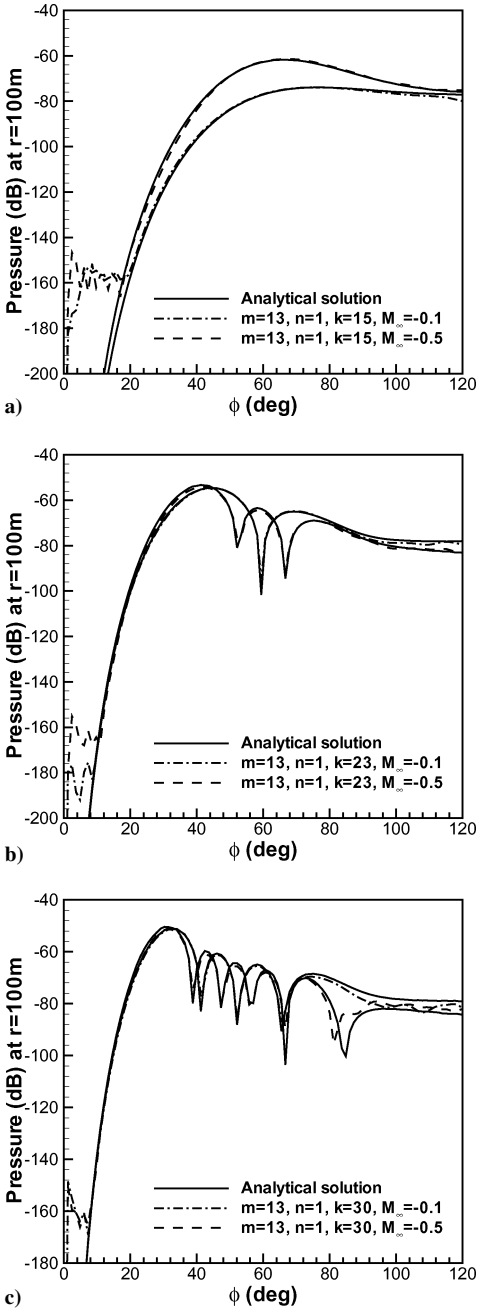

Fig. 8 Effect of mean flow on far-field directivity: a) $m, n = 13, 1, k = 15$, $\xi = 1.16$; b) $m, n = 13, 1, k = 23, \xi = 1.78$; and c) $m, n = 13, 1, k = 30, \xi = 2.32$.

To test the effect of the integral surface placement, we use the $m = 13$, $k = 30$, and $M_\infty = -0.5$ case. A series of spherical integral surfaces are constructed, centered on the center of the exit of the duct. Results in terms of the far-field directivity are given in Fig. 11a. There is very little difference in the main radiation peaks and the interference dip angles, suggesting a degree of insensitivity of the prediction to the surface placement. There are some slight changes in the low observation angle leakage and additional wiggles at the high observation angle as the integral surface is moved away from the duct. This feature suggests that the dispersion errors of the numerical scheme contribute to the low angle leakage. The overall effect, though, is rather small.

For the resolution study, we use the $m = 13$, $k = 30$, and $M_\infty = 0$ case. The unstretched calculation has a grid with $2\pi/(k_r \Delta y) = 13.5$ and $2\pi/(k_a \Delta x) = 11.3$. The stretched calculation concentrates cells near the wall and the duct exit, with $2\pi/(k_a \Delta x_{\min}) = 25$ and $2\pi/(k_r \Delta y_{\min}) = 30$, while maintaining the minimum resolution requirement away from the duct exit. Results are given in Fig. 11b. It

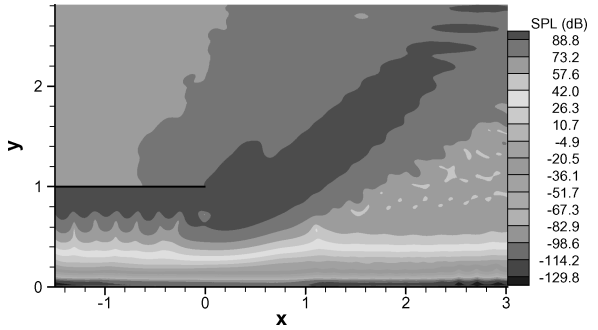

a) SPL at $k = 23$: $M_\infty = -0.1$

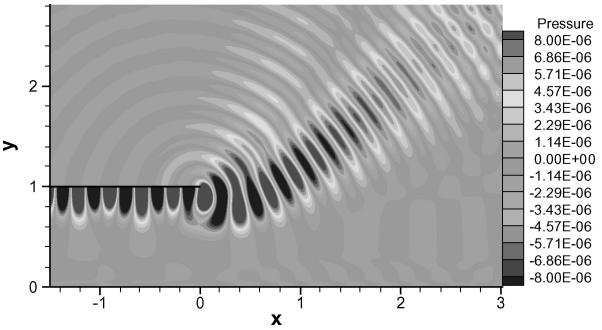

c) Pressure at $k = 23$: $M_\infty = -0.1$

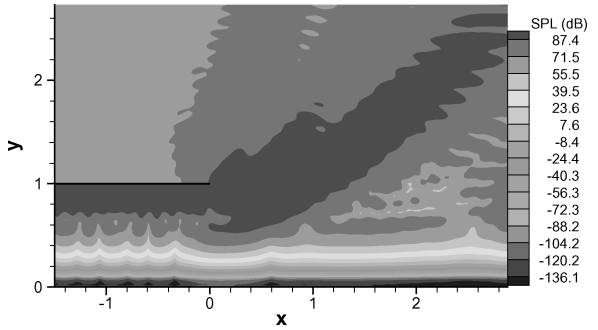

b) SPL at $k = 23$: $M_\infty = -0.5$

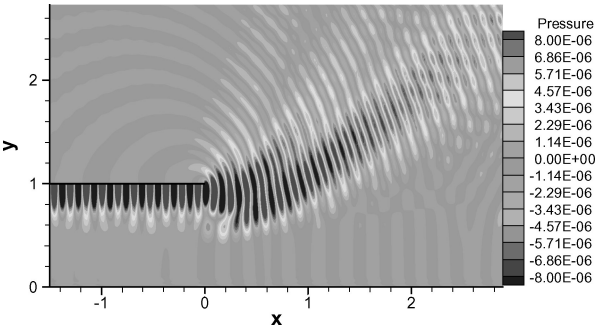

d) Pressure at $k = 23$: $M_\infty = -0.5$

Fig. 9 Pressure and SPL: m, $n = 13$, 1 modal radiation.

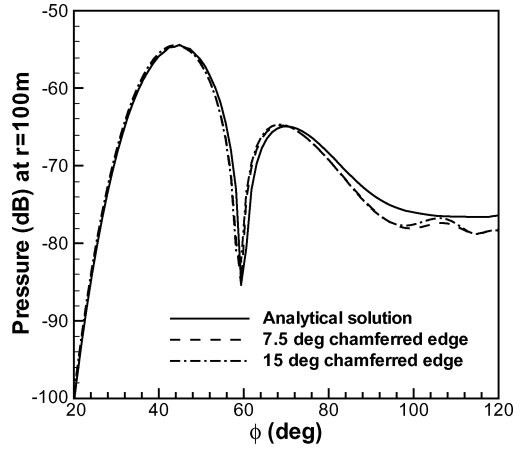

a) Chamfered edge

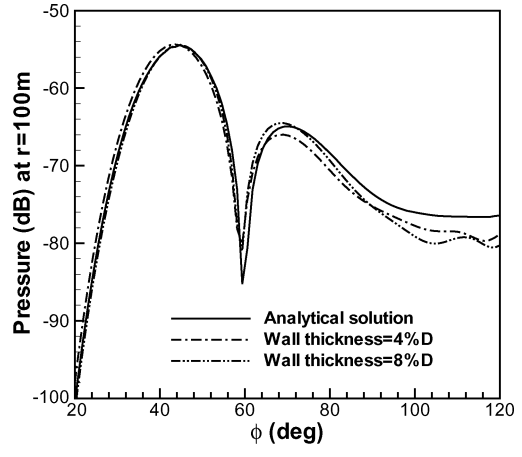

b) Wall thickness

Fig. 10 Effect of duct exit geometry on the far-field directivity prediction: $m = 13$, $n = 1$, $k = 23$, and $M_\infty = 0$.

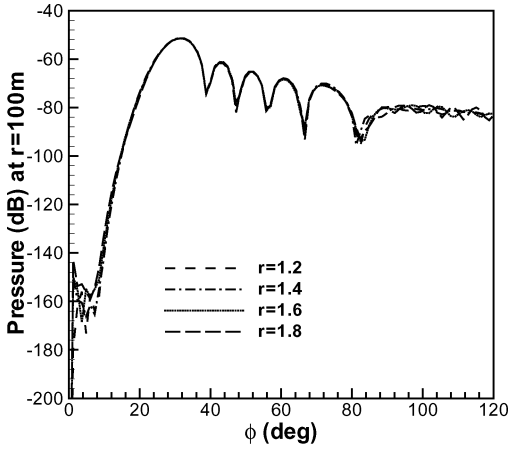

a) $m = 13$, $n = 1$, $k = 30$, $M_\infty = -0.5$

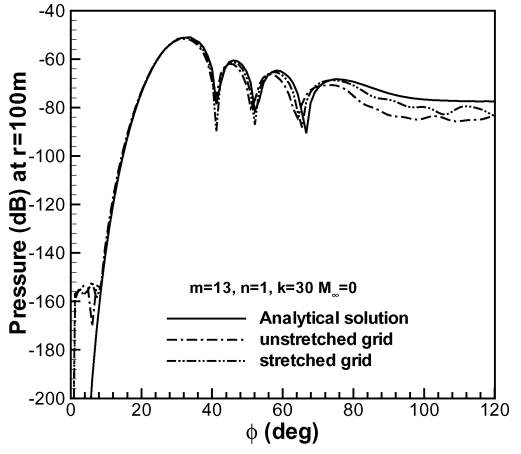

b) $m = 13$, $n = 1$, $k = 30$, $M_\infty = 0$

Fig. 11 Effect of a) grid and b) placement of the FW-H surface.

can be seen that the main radiation peak is predicted well, as well as the low angle values. However, a discrepancy is introduced at the higher angle and this discrepancy becomes progressively larger as the observation angle is increased. This result reproduces the deterioration in the far-field directivity prediction observed earlier. This suggests that the insufficient resolution near the duct exit is the main cause of the discrepancy.

VI. Conclusions

A numerical method is proposed for prediction of high-order spinning-mode radiation from an unflanged duct, with or without an arbitrary axisymmetric mean flow. The method is based on solutions of the linearized Euler equations for propagation inside the duct and near field and acoustic analogy for radiation. A formulation of the linearized Euler equations is proposed to accommodate a single azimuthal mode (2.5-dimensional equations).

Using a test case of high-order spinning-mode propagation inside an infinite duct, the resolution requirement is established. A minimum of seven to eight points per wavelength is required in both the axial and the radial directions to capture the correct wave propagation. However, an additional minimum points per wavelength requirement of 30 near the wall is also needed for the high-order spinning-mode propagation.

The numerical method has been tested against an analytical solution for modal radiation from an unflanged duct, under various conditions. Good agreement is demonstrated with analytical solution. The current numerical method can predict the far-field noise level with a 100-dB dynamic range.

Acknowledgments

This work is partly funded by the EU TurboNoiseCFD Project, Project GRD1-1999-10509. The authors thank Jeremy Astley and Sjoerd W. Rienstra for helpful discussions and assistance during the course of the study.

References

[1]Lidoine, S., Batard, H., Troyes, S., Delnevo, A., and Roger, M., "Acoustic Radiation Modelling of Aeroengine Intake Comparison Between Analytical and Numerical Methods," AIAA Paper 2001-2140, May 2001.

[2]Eversman, W., "Mapped Infinite Wave Envelope Elements for Acoustic Radiation in a Uniformly Moving Medium," *Journal of Sound and Vibration*, Vol. 224, 1999, pp. 665–687.

[3]Astley, R., Hamilton, J., Baker, N., and Kitchen, E., "Modelling Tone Propagation from Turbofan Inlets—The Effect of Extended Lip Liners," AIAA Paper 2002-2449, June 2002.

[4]Özyörü, Y., and Long, L., "Computation of Sound Radiating from Engine Inlet," *AIAA Journal*, Vol. 34, No. 5, 1996, pp. 894–901.

[5]Ahuja, V., Özyörü, Y., and Long, L., "Compuational Simulations of Fore and Aft Radiation from Ducted Fans," AIAA Paper 2000-1943, June 2000.

[6]Ffowcs Williams, J. E., and Hawkings, D. L., "Sound Generation by Turbulence and Surfaces in Arbitrary Motion," *Philosophical Transactions of the Royal Society of London*, Vol. 246, 1969, pp. 321–342.

[7]Farassat, F., and Succi, G. P., "The Prediction of Helicopter Discrete Frequency Noise," *Vertica*, Vol. 7, No. 4, 1983, pp. 309–320.

[8]Singer, B. A., Lockard, D. P., and Lilley, G. M., "Hybrid Acoustic Predictions," *Computers and Mathematics with Applications*, Vol. 46, No. 4, 2003, pp. 647–669.

[9]Homicz, G. F., and Lordi, J. A., "A Note on the Radiative Directivity Patterns of Duct Acoustic Modes," *Journal of Sound and Vibration*, Vol. 41, 1975, pp. 283–290.

[10]Brentner, K. S., and Farassat, F., "An Analytical Comparison of the Acoutstic Analogy and Kirchhoff Formulation for Moving Surfaces," *AIAA Journal*, Vol. 36, No. 8, 1998, pp. 1379–1386.

[11]Chen, X., Zhang, X., Morfey, C. L., and Nelson, P. A., "A Numerical Method for Noise Radiation from an Unflanged Duct," IMA Conf. on Computational Aeroacoustics, April 2002.

[12]Hixon, R., "A New Class of Compact Schemes," AIAA Paper 98-0367, Jan. 1998.

[13]Hu, F. Q., Hussaini, M. Y., and Manthey, J., "Low-Dissipation and -Dispersion Runge–Kutta Schemes for Computational Acoustics," *Journal of Computational Physics*, Vol. 124, 1996, pp. 177–191.

[14]Kennedy, C. A., and Carpenter, M. H., "Comparison of Several Numerical Methods for Simulation of Compressible Shear Layers," NASA TP 3484, Dec. 1997.

[15]Ashcroft, G., and Zhang, X., "Optimized Prefactored Compact Schemes," *Journal of Computational Physics*, Vol. 190, 2003, pp. 459–477.

R. So
Associate Editor